Variation in XANES in biotite as a function of orientation, crystal composition and metamorphic history: Revision 2

Evans, K.A.,[1] M. Darby Dyar,[2] Steven M. Reddy[1], Antonio Lanzirotti,[3]
David T. Adams[4] and Nick Tailby[5]

July 3, 2013

Abstract

Microscale analysis of ferrous:ferric iron ratios in silicate minerals has the potential to constrain geological processes but has proved challenging because textural information and spatial resolution are limited with bulk techniques, and in-situ methods have limited spatial resolution. Synchrotron methods, such as XANES, have been hampered by the sensitivity of spectra to crystal orientation and matrix effects.

In an attempt to break this nexus, biotites from Tanzania were characterised with a combination of optical microscopy, electron microprobe,

---

[1] Dept. Applied Geology, Curtin University, GPO Box U1987, Bentley, WA6845, Australia
[2] Mt. Holyoke College, Massachusetts, USA
[3] University of Chicago, Centre for Advanced Radiation Sources, Chicago, IL 60637 USA
[4] CMCA, UWA, Perth, Australia
[5] ecr

Mössbauer analysis, Electron Back Scatter Diffraction (EBSD) and X-ray Absorption Near Edge Structure (XANES) spectroscopy. Pre-edge and edge characteristics of the Fe Kα absorption feature were compared to orientation information derived by EBSD and ferric iron content derived from Mössbauer analysis.

Statistically significant correlations between measured spectral features and optic/crystallographic orientation were observed for individual samples. However, orientation corrections derived from these correlations did not reduce the uncertainty in $\mathrm{Fe}^{3+}/\mathrm{Fe}_{\mathrm{tot}}$. The observations are consistent with matrix- and ordering-dependency of the XANES features, and further work is necessary if a general formulation for orientation corrections is to be devised. (185 words)

Keywords: Fe, oxidation, XANES, biotite, orientation

Introduction

The oxidation state of iron in minerals is a critical control on mineral properties and is a strong determinant of the oxidation state of the host rock, which in turn, affects parameters such as rheology (Mackwell et al., 1990; Keefner et al., 2011), melting characteristics (Wyllie, 1995; Foley, 2011), and the release of elements of environmental and economic interest (e.g. S, C, Cu, Au) by melting and devolatilisation (Mavrogenes and O'Neill, 1999; Jugo et al., 2005; Jugo, 2009).

$\mathrm{Fe}^{3+}/\mathrm{Fe}_{\mathrm{tot}}$ in minerals can vary on a micron scale (Schmid et al., 2003; Delaney et al., 1998; Berry et al., 2010), and acquisition of this information could provide invaluable information on geological processes. However, measurement of $\mathrm{Fe}^{3+}/\mathrm{Fe}_{\mathrm{tot}}$ is challenging. Wet chemical and bulk Mössbauer methods (Meyrowitz, 1963; Li et al., 2005) require a bulk sample and so cannot resolve micron scale spatial variation of $\mathrm{Fe}^{3+}/\mathrm{Fe}_{\mathrm{tot}}$. In-situ Mössbauer has the potential to reach 50 micron spatial resolution, but the measurements are time-consuming and impractical for detailed studies of within-grain $\mathrm{Fe}^{3+}/\mathrm{Fe}_{\mathrm{tot}}$ variation (McCammon et al. 2004, McCammon 2005). EELS (Electron Energy Loss Spectroscopy) also has potential (e.g. Garvie et al., 2004; Keast et al., 2001) but requires a TEM thickness sample, so textural information is often lost during sample preparation.

Synchrotron XANES-based methods provide a promising opportunity for in-situ $\mathrm{Fe}^{3+}/\mathrm{Fe}_{\mathrm{tot}}$ analysis on beamlines with micro-focus capability. Spatial resolution is typically less than 10 microns and potentially less than 1 μm on the new high-resolution beamlines. Analysis can be achieved in minutes to tens of minutes, even at iron concentrations less than one weight percent. Early work provided calibrations based on the position of the centroid of the 1s to 3d Fe K pre-edge peak for iron in octahedral compounds (Bajt et al., 1994) and glasses (Berry et al., 2003, 2004). Further study revealed that the characteristics of the pre-edge peak are a complex function of site geometry, co-ordination, matrix composition, and mineral orientation. These functional relationships have been studied by a combination of experimental and theoretical methods (Randall et al., 1995; Arrio et al., 2000; Dyar et al., 2001, 2002a,b; Petit et al., 2001;

Wilke et al., 2004, 2005; Delaney et al., 2005; Wilke et al., 2007).

Results from these studies indicate that, for minerals with a high-spin electron arrangement such as biotite, the pre-edge peak intensity is mostly a function of the extent of electric dipole coupling induced by hybridisation of the 3d-4p orbitals, because the 1s to 3d transition is forbidden unless hybridisation occurs. Such hybridisation is facilitated by non-centrosymmetric site geometries for iron and thus peak intensities are higher for tetrahedrally coordinated than for octahedrally coordinated iron. The asymmetry of coordination polyhedra is also enhanced when bond lengths decrease. So, pre-edge peaks for Fe^{3+} are more intense than those for Fe^{2+} because the higher charge on Fe^{3+} results in shorter Fe-O distances. The more intense pre-edge peaks for Fe^{3+} are also caused by the greater probability of $1s$ to $3d$ transitions for Fe^{3+}, which occurs because there are more vacancies in the *d* levels for the higher valence oxidation state.

There is a broad correlation between pre-edge peak energy and oxidation state. Electrons are more tightly held in Fe^{3+} because of the greater charge, so transitions related to this oxidation state are at slightly higher energy (1-2 eV) than for Fe^{2+}. The number of sub-peaks in the composite pre-edge can be predicted via molecular orbital (MO) calculations (Rehr et al., 2009; Westre et al., 1997b). Octahedral Fe^{2+} should have three peaks, while tetrahedral Fe^{2+} has four. Octahedral Fe^{3+} and tetrahedral Fe^{3+} should both have two peaks, but only those for octahedral Fe^{3+} are expected to be resolvable. Tetrahedral Fe^{3+} is expected to produce a single intense peak because the separation of the two sub-peaks is small (< 0.7 eV). However, with typical configurations for

X-ray spectroscopy it is difficult to deconvolute XANES pre-edge peak information properly for minerals such as biotite with octahedral and tetrahedral ferric and ferrous iron, because spectrometer resolution, even with a high resolution monochromator, is insufficient.

The difficulty associated with resolution of individual peaks within the pre-edge peak for specific mineral phases means that existing calibrations (Wilke et al., 2001; Berry et al., 2003, 2004; Wilke et al., 2007, 2009), are largely empirical, although if the Fe co-ordination is known then plots of the type first reported by Wilke et al. (2001) can be used as a generalised calibration for the pre-edge peak. An empirical calibration for Fe^{3+}/Fe_{tot} in garnet (Berry et al., 2010) that uses main edge and post-main edge features has also been produced, and, at least for garnet, the main edge calibrations are more sensitive and provide higher precision than those based on pre-edge features. However, features at and above the main edge are strongly related to structural environment and thus display greater matrix dependence than pre-edge features, which record local environment to a greater extent. Existing calibrations allow accurate and precise measurements of Fe^{3+}/Fe_{tot} in isotropic or powdered material, so long as excellent matrix-matched calibration standards are available. It is also possible to make measurements of relative Fe^{3+}/Fe_{tot} within single anisotropic grains (Schmid et al., 2003; Vidal et al., 2006; Munoz et al., 2006). However, measurement of absolute Fe^{3+}/Fe_{tot} in-situ for anisotropic grains is still hampered by uncertainties related to matrix composition and crystal orientation (Dyar et al., 2001, 2002a) which limit precision in Fe^{3+}/Fe_{tot} to $10 - 15\%$ absolute. Brouder

(1990) derives and presents relationships between X-ray absorbance and crystal orientation for a wide range of crystal symmetries. It is therefore theoretically possible to account for orientation effects if crystal orientation is known.

Electron Back Scatter Diffraction (EBSD) provides a non-destructive way to precisely and accurately determine the orientation of crystals accurately with respect to a sample reference frame, and it is therefore possible that combination of this technique with XANES could eliminate, or substantially reduce, crystal orientation-related uncertainties in $\mathrm{Fe}^{3+}/\mathrm{Fe}_{\mathrm{tot}}$. In this study, we examine the characteristics of XANES spectra as a function of EBSD-derived mineral orientation, and assess the potential utility of the combined technique. Biotite grains from three samples are characterised using microprobe, Mössbauer, XANES and EBSD. Pre-edge peak and main edge XANES features were examined, and relationships between the areas of the component peaks and orientation parameters were investigated, and the potential for quantitative predictive calibrations assessed.

Material and Methods

The criteria for sample selection were that: the samples should contain significant modal proportions of biotite with homogeneous composition; the samples should not contain excessive magnetite that could contaminate the picked minerals; and that samples should cover a range of ferromagnesian assemblages, with the expectation that this would produce a range of ferric:ferrous ratios in the biotites. Three samples were chosen from a suite of partially retrogressed eclogites and granulites from western Tanzania. Samples T01-23 (S07^{o}08'7.2" E036^{o}08'10.9") and T01-28A (S07^{o}07'49.0" E036^{o}07'22.4") are Palaeoproterozoic metamorphic rocks of the Isimani Unit of the Usagaran Orogen (Reddy et al., 2003; Collins et al., 2004). Both samples are high-grade quartzo-feldspathic gneiss that show minor signs of lower grade metamorphic overprints (e.g. trace epidote and actinolite). ^{40}Ar/^{39}Ar data from micas in this region record an isotopic disturbance consistent with a weak Pan-African greenschist facies thermal overprint (Reddy et al., 2004). Sample T01-54 (S07^{o}34'44.0" E036^{o}45'45.0") is a strongly foliated banded gneiss comprising alternating layers of amphibole-rich and amphibole-poor quartzo-feldspathic layers. The sample analysed contains red-brown biotite, garnet and amphibole, plagioclase, K-feldspar and quartz. The sample was collected from the road section adjacent to the Great Ruaha River, close to the entrance of the Udzungwa Mountains National Park and is probably a Neoarchaean protolith reworked at high-grade conditions during Neoproterozoic Pan-African orogeny (Vogt et al., 2006).

Each sample was crushed for about 5 seconds in a tungsten carbide TEMA mill to produce grains a few hundred microns in size. The crushed sample was then passed repeatedly through a Frantz magnetic separator to concentrate the ferromagnesian fraction. 30 micrograms of biotite was hand-picked from each sample for Mössbauer analysis. Microprobe analysis, EBSD and XANES analysis were performed on polished thin sections. Thin sections were prepared in the normal way, plus a final polish with 0.06 μm colloidal silica NaOH suspension (pH 9.8) for ca. 2 hours on a Buehler Vibromet II polisher. A thin ($\sim$ 5 nm) carbon coat was applied before EBSD analyses to reduce surface charging.

Mineral composition analysis

Mineral compositions were analysed using the JEOL JXA-8530F hyperprobe located at the CMCA (Centre for Microscopy, Characterisation and Analysis) at the University of Western Australia. Accelerating voltage was 15 KeV, and the beam current was 20nA. Cation occupancies were calculated using the Ax software (Holland, pers. comm.)

Mössbauer

Approximately 30 mg of the sample was crushed to a fine powder with sugar under acetone before mounting in a sample holder confined by sellotape. Mössbauer spectra were acquired at 295K using a source of 80 mCi 57Co in Rh on a WEB Research Co. model WT302 spectrometer (Mount Holyoke College). Run times were $6 - 24$ hours, and results were calibrated against α-Fe foil; baseline counts ranged from $2 - 8$ million.

Mössbauer spectra were modeled using the Mex-Fieldd program, which was acquired from the University of Ghent courtesy of E. DeGrave. The program uses Lorentzian line shapes and solves full Hamiltonians for isomer shift and quadrupole splitting. Errors are 0.02 mm/s on isomer shift and as high as 0.05

mm/s for quadrupole splitting (Dyar et al., 2008). Errors on Fe^{3+}/Fe_{tot} are 1-3% absolute based on repeated fits to the same spectra. Doublet areas are assumed to correspond directly to the abundances of the species present (but see Dyar et al. (2008)).

Two of the samples appeared to contain a small amount of impurity that is a magnetic phase; only the center two peaks of the sextet are visible at this velocity range. Their locations suggest that this phase is hematite, which is weakly magnetic. However, the emphasis of this work is to use Mössbauer spectroscopy to determine the ferric iron proportion in biotite so confirmation of this suggestion is not necessary.

EBSD

EBSD mapping was undertaken at the Microstructural Analysis Facility, Curtin University, Western Australia, using a W-source Philips XL30 SEM operating at 20 kV and a 15 mm working distance. The SEM is fitted with a Nordlys I EBSD acquisition camera, two forescatter OCI detectors, and an Oxford Instruments (formerly HKL Technologies) EBSD system. All EBSD data were acquired and processed using Oxford Instruments Channel 5 (SP9) software.

Biotite has significant issues with multiple solutions because of the pseudo threefold axis around the pole to (001), i.e. <103>. Such pseudosymmetry issues can create significant systematic misindexing of EBSD data. To reduce the effect of this misindexing problem the camera distance was selected to increase the number of visible Kikuchi bands within each diffraction pattern. Prior to data collection individual diffraction patterns were collected and calibrated manually using >7 bands and solutions were checked against the empirically-derived electron backscatter pattern (EBSP). During this process it became clear that recognition of the correct solution is not possible by visually comparing solutions with the EBSP. To facilitate the correct identification of biotite lattice orientation multiple analyses of the biotite grains using automated mapping was employed. Following this mapping, data were noise reduced to remove isolated points with anomalous orientations from the data using the Tango wildspike correction tool, and a 6 nearest-neighbour extrapolation to reduce the proportion of zero solutions.

XANES

XANES spectra were collected at beamline X26A at the National Synchrotron Light Source (NSLS), which is sited at the Brookhaven National Laboratory, Upton, New York, USA. Energy scans were made across the Fe K edge in four regions: (i) from 7020 to 7096eV in 10eV steps with a 1 second counting time; (ii) from 7096 to 7118 eV, which is the pre-edge peak region, with 0.1 eV steps and five second count time; (iii) from 7118.2 eV to 7140 eV in 0.4 eV steps and 2 second count time; and finally (iv) from 7141 to 7220 eV in 3 eV steps with a 2 second count time. Spectra collection for each sample required approximately 30 minutes. The beam was located and beam size assessed by scans across the edge of a razor blade. Beam size was measured to be 7 μm x 11μm, with the larger dimension in the horizontal plane; the beam was also highly polarised to produce an electric vector lying in the horizontal plane. The extent of polarisation was not measured but for an NSLS bending magnet source is assumed to be $> 96\%$ (Janssens et al., 1993). Beam energy was tuned by a Si(311) lattice, channel-cut, monochromator, the crystals are cut to a 7 mm gap and cooled to 11^{o}C using a Neslab chiller. The Si(311) with a 0.2 mm upstream aperture has an instrumental resolution of 0.36 eV at 6 keV. Adding this resolution in quadrature with the natural Fe K width for the 1s electron level of 1.08 eV (Krause and Oliver, 1979), and accounting for instrumental broadening of the overall resolution yields an overall resolution of 1.3 eV. Microfocus is achieved via a pair of 100 mm long rhodium-coated, grazing-incidence silicon mirrors in a Kirkpatrick-Baez (KB) geometry. Photon flux at 7 keV is roughly 2.5x10^8 photons second^{-1} with the Si(311) monochromator. A 5X Mitutoyo long working distance objective with CCD digital image capture is mounted horizontally so that the sample surface can be viewed normally.

Energy calibration was performed against samples of NMNH (National Museum of Natural History) magnetite and Balmat magnetite. Calibration was based on the assumption that the centroid of the magnetite pre-edge peak was at 7113.25 eV. Use of natural magnetites as reference standards requires caution because natural samples with appreciable Cr and Ti may not be fully ordered in the inverse spinel structure with all Fe^{2+} on the octahedral site (Wilke et al., 2001). If this is the case then the centroid position could vary from sample to sample. However, in this case, the Balmat and NMNH magnetites were measured sequentially and found to have identical Fe K pre-edge and main-edge absorption energies, within the resolution of the system. Magnetite standards were run after every beam fill, and every three to five samples to monitor for any energy drift. Energy corrections were performed assuming that any monochromator drift involved a linear relationship between time and drift between standard measurements as photon flux decreased relative to decaying current in the NSLS X-ray storage ring. Total drift over the two day run was 0.25 eV. Spectra were collected in a fluorescence geometry, and the thin sections were mounted vertically at 45 degrees to the beam direction. After spectra from each grain of interest on the thin section had been collected, the sample was rotated by 90° within the plane of the section and a second spectra was collected. Fluorescent X-rays were detected using a 9-element Canberra high purity germanium (HPGe) detector. Count rates were normalised to the incident beam current and corrected for dead time.

Data Processing

Spectra were corrected for monochromator energy drift using the Balmat magnetite analyses described above. The background was removed and the signal was normalised using the Athena software (Ravel and Newville, 2005). Normalisation involved division of the signal by an estimation of the signal at the edge energy, taken to be 7120 eV. The estimated signal is calculated from the difference between pre-edge and post-edge lines extrapolated to 7120 eV. The pre-edge line was constructed by regression of the data between 7050 and 7090 eV. The post-edge line is a quadratic polynomial regressed to the data between 35 and 100 eV above the edge. These values were chosen to encompass a single oscillation in the post-edge spectra.

The biotite is Fe-rich ($\sim$20 wt%) so self absorption must be considered. Absorption lengths were calculated using the Hephaestus software (Ravel and Newville, 2005) and the microprobe-derived mineral formulae and were found to be 60 microns in the pre-edge region and around 30 microns in the post-edge region. The contribution of iron to the absorption is around 10% in the pre-edge region and over 60% in the post-edge region. The thin sections are 30 microns thick and the angle between the beam and the sample was 45 degrees, so the effective thickness of biotite grains was a maximum of 42 microns. Thus, in the pre-edge region μt is around 0.7, whereas it around 1.4 in the main edge and post-edge regions. If self absorption is to be ignored then the element of interest needs to be relatively dilute or μt needs to be significantly less, or significantly greater than 1 (Pfalzer et al., 1999). The biotite analysed fulfils this criteria in the pre-edge region, since Fe contributes only 10% of the absorption. This conclusion is consistent with those of Bajt et al. (1994) and Berry et al. (2010). However, self-absorption is likely to affect main edge characteristics - see discussion in Berry et al. (2010) and below. Self-absorption may also affect magnetite spectra, even in the pre-edge. However, magnetite was only used as a monitor for monochromator calibration and each measurement would have suffered the same self absorption effects, so self absorption is not be a problem for this application.

Subsequent processing was performed using custom-built functions written in Mathematica$^{\mathrm{TM}}$. The pre-edge peak was extracted from the data by subtraction of a baseline. The baseline was derived from an arctan function fit to the data between 7100 and 7119 eV, excluding the peak which was considered to lie between 7109 eV and 7116.5 eV. Variations on the fit windows described above were tried and the chosen values were found to produce reproducible results for all three samples with minimal artefacts. The pre-edge peak was then fit to a combination of three Lorentzians in two stages. Initially, peak positions and areas were fit. In all fits, peak widths were constrained to 1.3 eV, the theoretical width derived from the monochromator resolution and values for core hole width at the Fe K edge. The most consistent fits were obtained with three component peaks; fits with two peaks could not reproduce the data, and fits to four peaks were non-unique and therefore underdetermined.

Fits that utilised pseudo-Voigt peaks were also attempted, where the pseudo-Voigt peak is constructed from the sum of a Gaussian and Lorentzian peak. Theoretically, Voigt or pseudo-Voigt peaks are better suited to XANES peak fitting than simple Lorentzians (Wilke et al., 2001). The Lorentzian contribution accounts for the true peak shape, while the Gaussian contribution is produced by peak broadening due to limitations in the experimental energy resolution. A number of strategies were tried that included Voigt peaks in the fit. First, the Mathematica routine was modified to fit to three Voigt peaks, with Gaussian broadening of 1.3 eV and Lorentzian broadening of 1.08 eV. Fits utilising these parameters were worse than those with simple Lorentzians. Fit attempts were also made specifying the Lorentzian broadening parameters as fit parameters. No improval in fit was noted and strict limits on the fit parameters were required as the system started to become underdetermined. If these limits were omitted then the fit parameters were often found to take physically unrealistic values. The inclusion of pseudo-Voigt peaks, where the peaks are constructed from a simple sum of Gaussian and Lorentzian terms was also considered. However, the number of fit parameters introduced by the need to specify Gaussian and Lorentzian proportions plus parameters to specify different peak widths for the two components meant that the data available was insufficient to uniquely determine the fit parameters. The failure of Voigt peaks to replicate the data any better than the simple sum of Lorentzians led to retention of the Lorentzians.

Peak positions from the preliminary fit for each sample were plotted on a histogram, and subsequent fitting exercises used the highest frequency peak energies from this histogram. The final fit to the data utilised these peak positions, and peak areas were fit for set peak positions and widths. This two-step strategy allowed a good combination of flexibility and consistency. Uncertainties were derived from the residuals to the non-linear regression and propagated to give uncertainties on the centroid and on the calculated $\mathrm{Fe}^{3+}/\mathrm{Fe}_{\mathrm{tot}}$. The position of the centroid was calculated from the peak areas and positions, and an estimate of the apparent proportion of ferric iron was made using the expression derived for micas by Dyar et al. (2001).

Additionally, the energy at a normalised peak intensity of 0.9 ($I_\mathrm{N} = 0.9$) was measured, after correction for any monochromator drift, and used as a potential calibration parameter. This was performed because Berry et al. (2010) found that $I_\mathrm{N} = 0.9$ in garnet correlated better with $\mathrm{Fe}^{3+}/\mathrm{Fe}_\mathrm{tot}$ than any of the pre-edge parameters. However, it should be noted that caution is necessary in the application of main edge features to calculate $\mathrm{Fe}^{3+}/\mathrm{Fe}_\mathrm{tot}$ because main edge features are much more sensitive to mineral characteristics on longer length scales than the individual atom, such as ordering and the identity of an atom's nearest neighbours. Main edge features are also more likely to suffer from issues related to self absorption.

Theory

EBSD results provided measurements of the orientations of the crystallographic axes, and of the angle between the a and c axes. This allowed the orientations of the indicatrix axes, α, β, and γ to be calculated. The angles between the electric vector (E) and the crystallographic and indicatrix axes, and [001], and were calculated using stereonets and the program OSXStereonet (Allmendinger et al., 2012).

The absorbance cross section due to the dipole transition in biotite, which belongs to the space group $C2/m$ is

$$\sigma^{\mathrm{D}}(\epsilon) = \sigma^{\mathrm{D}}(0,0) - \sqrt{3}\sin^2\phi_{\mathrm{Z}}\left[\cos 2\psi\sigma^{\mathrm{Dr}}(2,2) + \sin 2\psi\sigma^{\mathrm{Di}}(2,2)\right] - \left(\frac{1}{\sqrt{2}}\right)(3\cos^2\phi_{\mathrm{Z}} - 1)\sigma^{\mathrm{D}}(2,0) \tag{1}$$

(Brouder, 1990). $\sigma^{\mathrm{D}}(\epsilon)$ is absorbance as a function of the polarisation vector ϵ, $\sigma^{\mathrm{D}}(0,0)$ is the isotropic absorption cross section, which is the same as that which would be measured on powders. $\sigma^{\mathrm{D}}(2,0)$ is related to absorption of the most anisotropic section, and σ^{Dr}(2,2) and σ^{Di}(2,2) refer to real and imaginary parts of absorbance for (2,2) respectively. ϕ_{Z} is the angle between the Z axis of the absorbance ellipsoid and the electric vector and ψ is the angle of the electric vector with respect to the X axis of the absorbance ellipsoid (Figure 1).

Interpretation of the spectra using Eqn 1 is problematic, partly because of the pseudosymmetry issues encountered during the EBSD analysis, and partly because the unknown orientation of the absorbance ellipsoid relative to the indicatrix provides a number of unknowns too large to be determined with the dataset acquired for this study. However, fortunately, the symmetry is close to trigonal; α and γ diverge from the c and a axes respectively by less than 5 degrees for the samples studied here, and the β and γ refractive indices have very similar values, as indicated by the low birefringence of (001) sections. The absorbance cross-section due to electric dipole interactions for crystal symmetries with a rotation axis of order greater than two is

$$\sigma^{\mathrm{D}}(\epsilon) = \sigma^{\mathrm{D}}(0,0) - \left(\frac{1}{\sqrt{2}}\right)(3\cos^2\phi_{\mathrm{Z}} - 1)\sigma^{\mathrm{D}}(2,0) \tag{2}$$

Brouder (1990). Eqn 2 can be simplified to

$$\sigma^{\mathrm{D}}(\epsilon) = A1 + A2\cos^2\phi_{\mathrm{Z}} \tag{3}$$

where $A1$ is $\sigma^{\mathrm{D}}(0,0) - \frac{\sigma^{\mathrm{D}}(2,0)}{\sqrt{2}}$ and $A2$ is $\frac{3\sigma^{\mathrm{D}}(2,0)}{\sqrt{2}}$.

For this reason, preliminary interpretations of the data are made assuming that biotite symmetry is pseudo-trigonal and that Eqn 3 can be used to describe the relationship between crystal and absorbance orientation. In this case the z axis of biotite is assumed to be parallel to the Z axis of the absorbance ellipsoid and approximately parallel to the α axis of the absorbance ellipsoid. The β axis of the indicatrix is parallel to the b crystallographic axis, and to the Y axis of the absorbance ellipsoid. The γ axis of the indicatrix is assumed parallel to the a crystallographic axis, and to the X axis of the absorbance ellipsoid.

Additional absorbance may result from electric quadrupole interactions with the X-ray beam (Brouder, 1990). Theoretically, absorbance due to electric quadrupole interactions have been calculated to be around two orders of magnitude weaker than that for electric dipole interactions, and quadrupole absorbance has been neglected in a number of studies of the angular dependence of XAFS (e.g. Heald and Stern, 1977; Manceau et al., 1990; Dyar et al., 2002a; Berry et al., 2010). However, the 1s to 3d transition, which is invoked as the main cause of the Fe pre-edge peak (Shulman et al., 1976), is forbidden for complexes in centrosymmetric environments (Westre et al., 1997a). In such cases, quadrupole interactions can form a significant part of a weak pre-edge feature, as is observed for Cr^{3+} and V^{3+} in garnet (Cabaret et al., 2010). In non centrosymmetric environments, the mixing of 4p with 3d orbitals allows electric dipole 1s to 4p transitions, and it is this transition that dominates the pre-edge peak (e.g. Westre et al., 1997a). Brouder (1990) provides an equation for electric quadrupole interactions as a function of ϕ_Z and ψ. Ideally, it would be possible to assess the quadrupole interaction contribution to the pre-edge peak using this equation. However, the quadrupole equation contains four calibration parameters, and the signal is likely to be weak, due to the relatively asymmetric nature of the iron-bearing sites in biotite. Under these circumstances it was considered that the data set was insufficient to properly calibrate the electric quadrupole signal and this contribution to the pre-edge peak was not considered further.

To test the applicability of Eqn 3, the areas and proportions of the three Lorentzian peaks, the position of the centroid, and the energy of the normalised spectra at $\mathrm{I_N}$=0.9 were plotted against $\cos^2 \phi_\mathrm{Z}$, and correlation coefficients were calculated for each of the datasets.

Other potential orientation − XANES relationships were also tested. These included testing for a link between absorbance and the angle between the {110} lattice vectors and the electric vector, which is equivalent to testing for a relationship with ψ, as in Eqn 1. None of the more complex approaches produced results any better than those derived from the simple approach based on the assumption of pseudosymmetry, so only results based on Eqn 3 are presented here.

Results

The biotites measured (Fig. 2) were compositionally homogeneous (Table 1) both within grains and between grains in a thin section. Fe/(Fe+Mg) was between 0.46 – 0.56. Total Al varied between 1.3 and 1.5 cations per 11 oxygens, and calculated Ti was 0.15 to 0.22 cations per 11 oxygens. The highest Ti values occurred in the samples with red-brown biotite (T01-54). The site occupancy calculations did not indicate any ferric iron, or iron on the tetrahedral sites, but such calculations are not a reliable way to determine these parameters. The interlayer cation site was dominated by K with K/(K+Na) values greater than 0.99.

Results of the Mössbauer analysis (Table 1; Fig 3) indicate ferric iron proportions of 0.10, 0.23 and 0.21 for samples T01-23, T01-28, and T01-54 respectively. Fit diagnostics indicate an excellent fit of the model to the data (Table 4). The ferric iron content does not correlate with the Fe/(Fe+Mg) value, Al content or Ti content, or with the colour of the biotite. The two samples with the green-brown biotites (T01-23 and T01-28) had the lowest and highest ferric iron proportions respectively.

Despite the difficulty in polishing biotites for EBSD analysis, EBSPs for the biotites were of acceptable quality (e.g. Fig. 4a) and were routinely indexed by the Channel 5 software (Fig. 4b). For individual grains the proportion of points indexed successfully was generally greater than 50% (e.g. Fig. 4c). However, the indexed grains contain multiple solutions because of the pseudo-hexagonal symmetry of biotite (Fig. 4c). The different solutions represent 60 degree rotations around the pole to (001) and, as a result, poles to (001) record only a single solution (Fig. 4d).

In detail, the orientation of (001) poles is seen to vary systematically along small circles by up to 15 degrees (Fig. 4d). This is also reflected in the distribution of most of the other poles, with the exception of one pole, around which the other poles appear to be dispersed (Fig. 4d). This pattern of dispersion is commonly seen in minerals deforming by dislocation creep and can be interpreted in terms of the formation of tilt boundaries associated with the operation of particular slip systems (Reddy et al., 2007) associated with bending of the mineral lattice. In the case of biotite, deformation commonly occurs by slip on the (001) basal plane with <100> being a common Burgers vector. In this slip system scenario, the pole to (010) would be expected to be the axis about which all other poles are dispersed. In the example shown here, where the biotite grain is bent through about 15 degrees, only one of the (010) poles records no dispersion (Fig. 4d) so this must be the correctly indexed (010) pole. Consequently, the analysis of slightly bent grains provides an opportunity to overcome the inherent problem of systematic misindexing when trying to establish the orientation of biotite grains.

Even using the methodology outlined above, very few of the analysed biotites could be uniquely oriented because of the general absence of deformation within individual bioitite grains. Hence, most of the orientation data have uniquely oriented poles to (001) but less well-constrained {100} and {010} orientations.

Fortunately, ϕ_Z depends only on $\{001\}$ so the potential misindexing does not affect results acquired from Eqn 3.

XANES spectra showed significant variation in the characteristics of the pre-edge peak, main edge, and post-edge features between samples, between grains in a single sample, and as a function of orientation of individual grains (Fig. 5, Tables 5 – 7). A number of features showed consistent trends as a function of ϕ_Z if spectra collected at the highest and lowest values of ϕ_Z are compared. Spectra from samples oriented with a low ϕ_Z showed a smaller pre-edge peak, with, potentially, a slight skew to lower energy values, compared to spectra collected from samples oriented with a high ϕ_Z. The shape of the shoulder on the main edge also varied, and was found to occur at a higher normalised absorption for the spectra collected at low ϕ_Z. This feature may contribute towards variation in the value of the energy at a normalised intensity of 0.9 (I_N =0.9; Fig. 5a). With respect to edge and post-edge features, the total overall intensity of the second peak (MP2 on Fig. 5) is higher for the high ϕ_Z spectra, and the ratio of the intensities of the first two peaks, MP1:MP2, is lower for the high ϕ_Z spectra. Systematic differences continue at higher energies. The fall in energy after the third peak (MP3) occurs at higher energies for the spectra collected at low ϕ_Z. However, these systematic differences may be small relative to the variation between grains and between samples, because the relationships described above are not statistically significant if the full dataset is considered.

The isolated pre-edge peak data fit well to the combination of three Lorentzians (Fig. 6). The relative proportions of the three peaks vary with the angle between the electric vector and [001], and it appears, qualitatively, as though the sample out of any pair of measurements with a greater value for ϕ_{Z} also has a greater proportion of the pre-edge peak accommodated in the lowest energy peak, which is referred to as P1 (Figs 6a, c and e versus b, e and f). The middle and highest energy peaks are referred to as P2 and P3 respectively, but there is little sign of a systematic relationship between the proportions of these peaks and the grain orientation. Additionally, while the general trend of the differences in relative peak area between measurements on a single grain seems reasonably consistent, there appears to be significant variation between grains and between samples.

The preliminary peak fitting exercise revealed three relatively well separated groups of Lorentzian positions (Fig. 7). The P1 peak at 7111.4 eV was well defined and in the same position for all three samples. The P2 peak varied more and samples T01-23 and T01-28 was at slightly lower energies (7112.1 – 7112.9 eV) than for T01-54 (7112.7 – 7113.1 eV). A similar trend was observed for the P3 peak, with the bulk of measurements for T01-23 and T01-28A at 7113.3 – 7114.1 eV and T01-54 at 7114.1 – 7114.4 eV. The similarity of T01-23 and T01-28A, and the difference between these samples and T01-54 is not related to the Mössbauer-derived estimates of $\mathrm{Fe}^{3+}/\mathrm{Fe}_{\mathrm{tot}}$ (Table 4), which indicate that T01-28A and T01-54 have very similar ferric iron contents whereas that of T01-23 is significantly less. However, T01-54 does differ in having significantly higher Ti content (Table 3).

Ferric iron contents calculated using the formula of Dyar et al. (2001) are within error of the values measured by Mössbauer (compare Table 4 to Tables 5 to 7). However, the uncertainties are relatively large, and there is no significant difference between T01-23, which has Mössbauer-derived Fe^{3+}/Fe_{tot} of 0.1, and the other two samples, which have Mössbauer-derived values of Fe^{3+}/Fe_{tot} of around 0.22. The standard deviation of the measurements of centroid and Fe^{3+}/Fe_{tot} for grains within a sample is much larger than the propagated error on the individual measurements, which indicates that the observed variation as a function of crystal orientation is real and not simply derived from uncertainties associated with analysis and the fitting process.

Calculated correlation coefficients (Table 8) show that the measured parameter that has the most convincing relationship with $\cos^2\phi_Z$ is the energy at $I_N = 0.9$, which correlates significantly with $\cos^2\phi_Z$ for two of the three samples and with a p value of less than 0.06 for the third (T01-54). The slope of the data in $\cos^2\phi_Z - I_N = 0.9$ space (Fig. 8a) was also similar for the three samples considered. T01-23 and T01-28A (low Ti samples), which have significantly different Fe^{3+}/Fe_{tot}, plotted in approximately the same region, while the higher Ti sample (T01-54) plotted at lower $I_N = 0.9$ values. There were no consistent significant, or nearly significant, correlations between $\cos^2\phi_Z$ and the measured centroid characteristics (e.g. Table 8; Figs 8b, c, d), though a significant correlation was observed between the area of P1 and $\cos^2\phi_Z$ for T01-28A ($p = 0.01$); a low p-value was calculated for the same pair of parameters for sample T01-54 (p=0.02). The other significant correlation was between the proportion of P3 and $\cos^2\phi_Z$ for T01-23 (p=0.009).

Discussion and Concluding Remarks

$I_{\mathrm{N}} = 0.9$ is the spectral characteristic that appears most reliably sensitive to crystal orientation (Fig. 8a). However, there doesn't seem to be any consistent relationship between the energy at $I_{\mathrm{N}} = 0.9$ and ferric iron content (Fig. 8a), although Berry et al. (2010) record a positive correlation between $\mathrm{Fe}^{3+}/\mathrm{Fe}_{\mathrm{tot}}$ and the energy at $I_{\mathrm{N}} = 0.9$ in garnet. It may be that $I_{\mathrm{N}} = 0.9$ is insensitive to biotite composition at the limits of resolution imposed by the analysis, or that additional factors related to the sample matrix contribute to the edge position and characteristics and obscure trends that might otherwise be discernible. The size of the error bars suggests the former. However, it is also useful to consider the potential effects of sample matrix.

It has been proposed that the shoulder on the main edge in biotite is caused by interactions between photoelectrons ejected from Fe atoms and neighbouring or second nearest neighbour Fe atoms, and that the characteristics of the feature record Fe-ordering (Dyar et al., 2001). The position and size of this shoulder affects $I_{\mathrm{N}} = 0.9$, so it is possible that the characteristics of the shoulder are sensitive to the composition of the matrix and depend on compositional parameters such as Fe/(Fe+Mg), the Al content of the biotite, the Ti content, as well as other factors such as the temperature of equilibration, which would affect the extent of ordering.

The temperature of equilibration, which affects ordering, also affects $\mathrm{Fe}^{3+}/\mathrm{Fe}_{\mathrm{tot}}$ in biotite via the stability of other minerals in the assemblage, if bulk rock

$\mathrm{Fe}^{3+}/\mathrm{Fe}_{\mathrm{tot}}$ is fixed or approximately fixed. This combination of causal links could produce a false correlation. For example, the presence of moderate quantities of epidote in the T01-23 sample could be interpreted to indicate that this sample equilibrated at a lower temperature than the other two, which are epidote-absent, and therefore have different ordering. Additionally, epidote, which contains ferric iron, may have sequestered ferric iron present in the rock so that the ferric iron in biotite is less than in the other two samples. Under these circumstances, temperature could have controlled both $\mathrm{Fe}^{3+}/\mathrm{Fe}_{\mathrm{tot}}$, and the energy at $I_{\mathrm{N}} = 0.9$ via mineral stability and ordering, respectively. In this case the presence or absence of correlation between the energy at $I_{\mathrm{N}} = 0.9$ and $\mathrm{Fe}^{3+}/\mathrm{Fe}_{\mathrm{tot}}$ should be treated cautiously.

Mineral assemblages do not provide evidence of a difference in temperature between the three samples examined. Sillimanite is present in T01-23 and T01-28A, while K-feldspar is present in T01-28A and T01-54. The presence of sillimanite indicates that the rocks equilibrated at temperatures in excess of 600°C for reasonable geothermal gradients, and the presence of K-feldspar indicates that temperatures were higher than the muscovite-out reaction which is consistent with temperatures higher than around 650°C, for these bulk compositions. Samples T01-23 and T01-28A were collected about 1500 m apart, and there is no evidence of a major structural discontinuity between them, while the T01-54 sample site is separated from the other two by a significant shear zone. The mineral assemblages in the three sections are too different and/or high variance for reliable comparative thermobarometry and a full pseudosection approach is beyond the scope of this paper. For this reason, the Ti-in-biotite geothermometer of Henry et al. (2005) was applied to obtain a preliminary assessment of temperature differences between the three samples. This geothermometer is empirically calibrated for rutile-bearing assemblages in aluminous metapelites and may, therefore, be unreliable for more mafic rocks such as T01-28A. Temperatures calculated for the three samples are 677 ± 20 °C for T01-23; 682 ± 20 °C for T01-28A, and 713° ± 20 C for T01-54. These temperatures are within uncertainty of each other, so it is not possible to confirm any significant difference in the temperature of equilibration between the three samples. However, differences in temperature may affect ordering, and hence XANES features, and this needs to be assessed in detail as part of any further development of the use of XANES to measure $\mathrm{Fe}^{3+}/\mathrm{Fe}_{\mathrm{tot}}$.

Features of the pre-edge peak, on which most attention has been focussed in previous work on $\mathrm{Fe}^{3+}/\mathrm{Fe}_{\mathrm{tot}}$, do not exhibit consistent relationships with crystal orientation (Table 8). The area of the P1 peak presents the best possibility, because significant or nearly significant correlations were observed for two samples (T01-23 and T01-54) but further work on this parameter is not useful because after orientation corrections only two points would be obtained, which are insufficient for determination of trends.

Orientation corrections

The simplest possible orientation correction is to fit the parameter of interest as a linear function of $\cos^2\phi_\mathrm{Z}$, (Eqn 3), and to project the parameter of interest to a chosen value of ϕ_Z. This correction was performed for the energy at $I_\mathrm{N} = 0.9$. The data were fit to

$$E_{I_\mathrm{N}=0.9} = m_1 \cos^2 \phi_\mathrm{Z} + c_1 \tag{4}$$

where $E_{I_\mathrm{N}=0.9}$ is the energy at $I_\mathrm{N} = 0.9$, and m_1 and c_1 are constants. Eqn 4 has the same form as Eqn 3. The data from each sample were fit to Eqn 4 to provide expressions that allow calculation of $E_{I_\mathrm{N}=0.9}$ as a function of ϕ_Z. The value chosen was 45^o, which is convenient because this value of ϕ_Z can be obtained if the cleavage of biotite in any $(hk0)$ section is aligned vertically during measurement. Values of the fit parameters, and their uncertainties are shown in Table 9.

Values of $I_\mathrm{N} = 0.9$ for $\phi_\mathrm{Z} = 45^o$ were plotted against Mössbauer-derived $\mathrm{Fe}^{3+}/\mathrm{Fe}_\mathrm{tot}$ (Fig. 9). The results should be treated with caution since there are only three data points, and two of these have similar $\mathrm{Fe}^{3+}/\mathrm{Fe}_\mathrm{tot}$ values; however, it can be seen that $I_\mathrm{N} = 0.9$ is not a function of $\mathrm{Fe}^{3+}/\mathrm{Fe}_\mathrm{tot}$.

Orientation correction parameters for each of the samples are different (Table 9). This supports the possibility discussed above, i.e. that XANES characteristics depend on factors other than orientation, such as biotite composition and the extent of ordering. This proposal is supported by the work of Wong et al. (1984) on vanadium spectra. Wong et al. (1984) recorded pre-edge peaks for octahedral trivalent V that were more intense when the V was held in roscoellite, a V-bearing mica, relative to those caused by V in V_2O_3. The difference was attributed to the fact that the Al neighbours of V in roscoellite are smaller and more highly charged than V neighbours. Bonds in roscoellite would therefore take on a more ionic character, and the probability of transitions into the $3d$ orbitals would be enhanced as these bonding orbitals would be, on average, more empty.

Under these circumstances, any biotite calibration, including the orientation correction, would have to be very closely matrix-matched, although relative changes in $\mathrm{Fe}^{3+}/\mathrm{Fe}_{\mathrm{tot}}$ within grains or between grains with similar compositions could be considered robust. The need for matrix correction is further supported by the distinctly different positions of the preliminary fit P2 and P3 Lorentzians (Fig. 7) for the green-brown Ti-poor biotites, T01-23 and T01-28A, and the red-brown Ti-rich biotite, T01-54. Further work, both experimental and theoretical, is necessary to elucidate the nature of the matrix-dependency.

Alternatively, it may be that the simplifying assumptions made in the development of the orientation correction are not justified and an improved orientation correction might be devised if the obstacles that necessitated the assumptions were removed. For example, it was assumed that the monoclinic biotite symmetry could be approximated by trigonal symmetry because this assumption greatly simplified the relationship between measured absorbance and crystal orientation, since in trigonal systems the axes of the absorbance ellipsoid are aligned with both the indicatrix axes and the [001] crystal axis.

If electric quadrupole interactions contributed significantly to the pre-edge peak then the use of Eqn 2 is inappropriate and a good fit of the data to the model would not be expected. Previous workers (e.g. Heald and Stern, 1977; Manceau et al., 1990; Dyar et al., 2002a; Berry et al., 2010) have neglected quadrupole interactions for fits of iron pre-edge peaks, and the large number of calibration parameters necessary to fit an electric quadrupole contribution to the data made it impossible to fit the data to the more complex model. However, in future, it would be informative to use ab-initio calculations to constrain the contribution of the electric quadrupole contribution, and perform a proper assessment on the likely significance of this feature.

It is also possible that orientation of the absorbance ellipsoid varies with the energy of the X-ray beam, since the different bonds which absorb at energies determined by crystal field splitting and symmetry constraints are oriented differently within the crystal. The detailed data needed to resolve the potentially complex nature of this problem was beyond the scope of the measurements made for this study, and indeed, the good correlations between orientation and key parameters such as $E_{I_{\mathrm{N}}=0.9}$ indicate that these effects are likely to be second order. However, further work focussed on measurement of the orientation of the absorbance ellipsoid might prove useful and allow reduction in orientation-related uncertainties.

It was also assumed that the beam was fully polarised, whereas, in reality, the use of the Kirkpatrick-Baez mirrors for focussing introduces a small degree of elliptical polarisation. Under these circumstances the electric vector has an additional orthogonal component. If the extent to which the synchrotron beam was elliptically polarised was known then it would be possible, though not trivial (compare Sambridge et al. (2008) to Libowitzky and Rossman (1996)), to develop equations for a two dimensional beam. If the extent of polarisation could be controlled then this feature could be used to constrain the orientation of the absorbance ellipsoid. However, the precise shape of the beam was not determined for this study.

It would also be possible to improve the resolution of the data if a standard were continuously monitored, such that the drift corrections did not involve interpolation in time. However, the drift corrections noted for this project were small relative to the variation in the energy at $I_{\mathrm{N}} = 0.9$ and the variation in centroid position so it is unlikely that the lack of an off-line standard had a serious impact on the quality of the results.

To summarise, pre-edge peak parameters do not correlate with biotite crystal orientation, but $E_{I_{\mathrm{N}}=0.9}$ is significantly correlated with ϕ_{Z} in two of the three samples and relatively well correlated in the third. Once the measurements are corrected for orientation, there is no significant relationship between $E_{I_{\mathrm{N}}=0.9}$ and $\mathrm{Fe}^{3+}/\mathrm{Fe}_{\mathrm{tot}}$. The absence of a correlation is attributed to composition- or temperature-related differences in ordering and/or simplifying assumptions used in the development of the model. Further work should include careful calibrations on matrix-matched standards and ab-initio modelling to assess the relative contributions of electric dipole and quadrupole to the pre-edge peak. If this work were performed then it may be possible to improve the precision and accuracy of synchrotron measurement of Fe^{3+}/Fe_{tot} in non-powdered samples.

Acknowledgements

The Australian Synchrotron Research Program is thanked for an Australian Synchrotron Research Fellowship to K. Evans. Portions of this work were performed at Beamline X26A, National Synchrotron Light Source (NSLS), Brookhaven National Laboratory. X26A is supported by the Department of Energy (DOE) - Geosciences (DE-FG02-92ER14244 to The University of Chicago - CARS). Use of the NSLS was supported by DOE under Contract No. DE-AC02-98CH10886. The AMMRF research program is thanked for travel funding. This work was also supported by ARC Discovery Grant DP1090475 and The Insitute for Geoscience Research at Curtin University (TiGeR). This is TiGeR publication number xxxx. An anonymous reviewer is thanked for a valuable contribution to the paper.

References

Allmendinger, R., Cardozo, N., and Fisher, D. (2012) Structural Geology Algorithms: Vectors and Tensors. Cambridge University Press, Cambridge.

Arrio, M.A., Rossano, S., Brouder, C., Galoisy, L., and Calas, G. (2000) Calculation of multipole transitions at the FeK pre-edge through p-d hybridization in the Ligand Field Multiplet model. Europhysics Letters, 51, 454–460.

Bajt, S., Sutton, S.R., and Delaney, J.S. (1994) X-Ray Microprobe Analysis of Iron Oxidation-States in Silicates and Oxides Using X-Ray-Absorption near-Edge Structure (Xanes). Geochimica Et Cosmochimica Acta, 58, 5209–5214.

Berry, A.J., O'Neill, H.S., and Foran, G.J. (2004) The in situ determination of redox states in silicate melts. Lithos, 73, S9–S9.

Berry, A.J., O'Neill, H.S., Jayasuriya, K.D., Campbell, S.J., and Foran, G.J. (2003) XANES calibrations for the oxidation state of iron in a silicate glass. American Mineralogist, 88, 967–977.

Berry, A.J., Yaxley, G.M., Woodland, A.B., and Foran, G.J. (2010) A XANES calibration for determining the oxidation state of iron in mantle garnet. Chemical Geology, 278, 31–37.

Brouder, C. (1990) Angular-Dependence of X-Ray Absorption-Spectra. Journal of Physics-Condensed Matter, 2, 701–738.

Cabaret, D., Bordage, A., Juhin, A., Arfaoui, M., and Gaudry, E. (2010) First-principles calculations of X-ray absorption spectra at the K-edge of 3d transition metals: an electronic structure analysis of the pre-edge. Physical Chemistry Chemical Physics, 12, 5619–5633.

Collins, A.S., Reddy, S.M., Buchan, C., and Mruma, A. (2004) Temporal constraints on Palaeoproterozoic eclogite formation and exhumation (Usagaran Orogen, Tanzania). Earth and Planetary Science Letters, 224, 175–192.

Delaney, J.S., Dyar, M.D., Gunter, M.E., Sutton, S.R., and Lanzirotti, A. (2005) Geometric constraints of in situ synchrotron micro-XANES determinations of oxidation state. Geochimica Et Cosmochimica Acta, 69, A793–A793.

Delaney, J.S., Dyar, M.D., Sutton, S.R., and Bajt, S. (1998) Redox ratios with relevant resolution: Solving an old problem by using the synchrotron microXANES probe. Geology, 26, 139–142.

Dyar, M.D., Delaney, J.S., and Sutton, S.R. (2001) Fe XANES spectra of iron-rich micas. European Journal of Mineralogy, 13, 1079–1098.

Dyar, M.D., Gunter, M.E., Delaney, J.S., Lanzarotti, A., and Sutton, S.R. (2002a) Systematics in the structure and XANES spectra of pyroxenes, amphiboles, and micas as derived from oriented single crystals. Canadian Mineralogist, 40, 1375–1393.

Dyar, M.D., Lowe, E.W., Guidotti, C.V., and Delaney, J.S. (2002b) Fe3+ and Fe2+ Partitioning Among Silicates in Metapelites: a Synchrotron Micro-Xanes Study. American Mineralogist, 87, 514–522.

Dyar, M.D., Schaefer, M.W., Sklute, E.C., and Bishop, J.L. (2008) Mossbauer spectroscopy of phyllosilicates: effects of fitting models on recoil-free fractions and redox ratios. Clay Minerals, 43, 3–33.

Foley, S.F. (2011) A Reappraisal of Redox Melting in the Earth's Mantle as a Function of Tectonic Setting and Time. Journal of Petrology, 52, 1363–1391.

Heald, S.M. and Stern, E.A. (1977) Anisotropic X-Ray Absorption in Layered Compounds. Physical Review B, 16, 5549–5559.

Henry, D.J., Guidotti, C.V., and Thomson, J.A. (2005) The Ti-saturation surface for low-to-medium pressure metapelitic biotites: Implications for geothermometry and Ti-substitution mechanisms. American Mineralogist, 90, 316–328.

Janssens, K., Vincze, L., Vanespen, P., and Adams, F. (1993) Monte Carlo simulation of conventional and synchrotrojn energy-dispersive x-ray spectrometers. X-Ray Spectrometry, 22, 234–243.

Jugo, P.J. (2009) Sulfur content at sulfide saturation in oxidized magmas. Geology, 37, 415–418.

Jugo, P.J., Luth, R.W., and Richards, J.P. (2005) An experimental study of the sulfur content in basaltic melts saturated with immiscible sulfide or sulfate liquids at 1300 degrees C and 1 center dot 0 GPa. Journal of Petrology, 46, 783–798.

Keefner, J.W., Mackwell, S.J., Kohlstedt, D.L., and Heidelbach, F. (2011) Dependence of dislocation creep of dunite on oxygen fugacity: Implications for viscosity variations in Earth's mantle. Journal of Geophysical Research-Solid Earth, 116.

Krause, M.O. and Oliver, J.H. (1979) Natural Widths of Atomic K-Levels and L-Levels,K-Alpha X-Ray-Lines and Several Kll Auger Lines. Journal of Physical and Chemical Reference Data, 8, 329–338.

Li, Y.L., Zheng, Y.F., and Fu, B. (2005) Mossbauer spectroscopy of omphacite and garnet pairs from eclogites: Application to geothermobarometry. American Mineralogist, 90, 90–100.

Libowitzky, E. and Rossman, G.R. (1996) Principles of quantitative absorbance measurements in anisotropic crystals. Physics and Chemistry of Minerals, 23, 319–327.

Mackwell, S.J., Bai, Q., and Kohlstedt, D.L. (1990) Rheology of Olivine and the Strength of the Lithosphere. Geophysical Research Letters, 17, 9–12.

Manceau, A., Bonnin, D., Stone, W.E.E., and Sanz, J. (1990) Distribution of Fe in the Octahedral Sheet of Trioctahedral Micas by Polarized Exafs - Comparison with Nmr Results. Physics and Chemistry of Minerals, 17, 363–370.

Mavrogenes, J.A. and O'Neill, H.S.C. (1999) The relative effects of pressure, temperature and oxygen fugacity on the solubility of sulfide in mafic magmas. Geochimica Et Cosmochimica Acta, 63, 1173–1180.

Meyrowitz, R. (1963) A semimicroprocedure for the detrmination of ferrous iron in nonrefractory silicate minerals. American Mineralogist, 48, 340–347.

Munoz, M., De Andrade, V., Vidal, O., Lewin, E., Pascarelli, S., and Susini, J. (2006) Redox and speciation micromapping using dispersive X-ray absorption spectroscopy: Application to iron chlorite mineral of a metamorphic rock thin section. Geochemistry Geophysics Geosystems, 7.

Petit, P.E., Farges, F., Wilke, M., and Sole, V.A. (2001) Determination of the iron oxidation state in Earth materials using XANES pre-edge information. Journal of Synchrotron Radiation, 8, 952–954.

Pfalzer, P., Urbach, J.P., Klemm, M., Horn, S., denBoer, M.L., Frenkel, A.I., and Kirkland, J.P. (1999) Elimination of self-absorption in fluorescence hard-x-ray absorption spectra. Physical Review B, 60, 9335–9339.

Randall, C.R., Shu, L.J., Chiou, Y.M., Hagen, K.S., Ito, M., Kitajima, N., Lachicotte, R.J., Zang, Y., and Que, L. (1995) X-Ray-Absorption Pre-Edge Studies of High-Spin Iron(Ii) Complexes. Inorganic Chemistry, 34, 1036–1039.

Ravel, B. and Newville, M. (2005) ATHENA, ARTEMIS, HEPHAESTUS: data analysis for X-ray absorption spectroscopy using IFEFFIT. Journal of Synchrotron Radiation, 12, 537–541.

Reddy, S.M., Collins, A.S., Buchan, C., and Mruma, A.H. (2004) Heterogeneous excess argon and Neoproterozoic heating in the Usagaran Orogen, Tanzania, revealed by single grain Ar-40/Ar-39 thermochronology. Journal of African Earth Sciences, 39, 165–176.

Reddy, S.M., Collins, A.S., and Mruma, A. (2003) Complex high-strain deformation in the Usagaran Orogen, Tanzania: structural setting of Palaeoproterozoic eclogites. Tectonophysics, 375, 101–123.

Reddy, S.M., Timms, N.E., Pantleon, W., and Trimby, P. (2007) Quantitative characterization of plastic deformation of zircon and geological implications. Contributions to Mineralogy and Petrology, 153, 625–645.

Rehr, J.J., Kas, J.J., Prange, M.P., Sorini, A.P., Takimoto, Y., and Vila, F. (2009) Ab initio theory and calculations of X-ray spectra. Comptes Rendus Physique, 10, 548–559.

Sambridge, M., Gerald, J.F., Kovacs, I., O'Neill, H.S.C., and Hermann, J. (2008) Quantitative absorbance spectroscopy with unpolarized light: Part I. Physical and mathematical development. American Mineralogist, 93, 751–764.

Schmid, R., Wilke, M., Oberhansli, R., Janssens, K., Falkenberg, G., Franz, L., and Gaab, A. (2003) Micro-XANES determination of ferric iron and its application in thermobarometry. Lithos, 70, 381–392.

Shulman, G.R., Yafet, Y., Eisenberger, P., and Blumberg, W.E. (1976) Observations and interpretation of x-ray absorption edges in iron compounds and proteins. Proceedings of the National Academy of Sciences of the United States of America, 73, 1384–8.

Vidal, O., De Andrade, V., Lewin, E., Munoz, M., Parra, T., and Pascarelli, S. (2006) P-T-deformation-Fe3+/Fe2+ mapping at the thin section scale and comparison with XANES mapping: application to a garnet-bearing metapelite from the Sambagawa metamorphic belt (Japan). Journal of Metamorphic Geology, 24, 669–683.

Vogt, M., Kroener, A., Poller, U., Sommer, H., Muhongo, S., and Wingate, M.T.D. (2006) Archaean and Palaeoproterozoic gneisses reworked during a Neoproterozoic (Pan-African) high-grade event in the Mozambique belt of East Africa: Structural relationships and zircon ages from the Kidatu area, central Tanzania. Journal of African Earth Sciences, 45, 139–155.

Westre, T.E., Kennepohl, P., DeWitt, J.G., Hedman, B., Hodgson, K.O., and Solomon, E.I. (1997a) A multiplet analysis of Fe K-edge 1s-¿3d pre-edge features of iron complexes. Journal of the American Chemical Society, 119, 6297–6314.

—— (1997b) A multiplet analysis of Fe K-edge 1s to 3d pre-edge features of iron complexes. Journal of the American Chemical Society, 119, 6297–6314.

Wilke, M., Farges, F., Petit, P.E., Brown, G.E., and Martin, F. (2001) Oxidation state and coordination of Fe in minerals: An FeK-XANES spectroscopic study. American Mineralogist, 86, 714–730.

Wilke, M., Partzsch, G.M., Bernhardt, R., and Lattard, D. (2004) Determination of the iron oxidation state in basaltic glasses using XANES at the K-edge. Chemical Geology, 213, 71–87.

—— (2005) Determination of the iron oxidation state in basaltic glasses using XANES at the K-edge (vol 213, 71, 2004). Chemical Geology, 220, 141–+.

Wilke, M., Farges, F., Partzsch, G.M., Schmidt, C., and Behrens, H. (2007) Speciation of Fe in silicate glasses and melts by in-situ XANES spectroscopy. American Mineralogist, 92, 44–56.

Wilke, M., Hahn, O., Woodland, A.B., and Rickers, K. (2009) The oxidation state of iron determined by Fe K-edge XANES-application to iron gall ink in historical manuscripts. Journal of Analytical Atomic Spectrometry, 24, 1364–1372.

Wong, J., Lytle, F.W., Messmer, R.P., and Maylotte, D.H. (1984) K-Edge Absorption-Spectra of Selected Vanadium Compounds. Physical Review B, 30, 5596–5610.

Wyllie, P.J. (1995) Experimental Petrology of Upper-Mantle Materials, Process and Products. Journal of Geodynamics, 20, 429–468.

Figure Captions

Figure 1: Schematic illustration of the absorption ellipsoid, showing the direction of the beam, the electric vector and angles discussed in the text.

Figure 2: Plane polarised photomicrographs of (a) T01-23; (b) T01-28A; (c) T01-54. Labels indicate the biotite grains analysed.

Figure 3: Results of Mössbauer spectroscopy on (a) T01-23; (b) T01-28A; (c) T01-54.

Figure 4. Electron backscatter diffraction data from biotite grain EB5 (Sample T01-23). a) Typical EBSP from the grain. Although the bands can be seen they are relatively faint due to the difficulty in polishing biotite. b) the indexed orientation derived from comparison of bands identified in (a) with a theoretical diffraction pattern for biotite. c) Orientation map created by applying red, green and blue colours to each of the 3 Euler orientations required to define the orientation of the lattice at each pixel. The variation in colour indicates an apparent change in orientation associated with a systematic misindexing due to the pseudo-hexagonal symmetry of biotite. d) pole figures for {100}, {010} and {001} for the grain shown in (c). Colours represent the orientations shown in (c) The misindexing is shown by the presence of three clusters in the {100} and {010} data. Only {001} shows a single orientation indicating that the misindexing represents an apparent 60 rotation around the {001} pole. The dispersion of data for

most of the poles by 15^o around small circles are consistent with deformation by dislocation creep. The absence of dispersion around the centrally located {010} pole, combined with the knowledge of biotite deformation mechanisms allows this pole to be identified as the real orientation of the grain despite the systematic misindexing problem (see text for details).

Figure 5. XANES. (a,b) absorption edge and pre-edge peak for T01-23; (c,d) absorption edge and pre-edge peak for T01-28A; (e, f) absorption edge and pre-edge peak for T01-54. Orientations chosen to show high and low ϕ_{Z} for a given grain.

Figure 6. Fit to pre-edge peak for spectra shown in Fig. 5 (a, b) T01-23; ((c, d) T01-28A; (e, f) T01-54. Dots indicate measured absorption values with background removed. Lines indicate the fit Lorentzian peaks.

Figure 7. Histogram illustrating the positions of Lorentzians obtained during preliminary pre-edge peak analysis.

Figure 8. Relationships between $\cos^2\phi_{\mathrm{Z}}$ and measured parameters for the three samples investigated. (a) Energy at $I_{\mathrm{N}} = 0.9$; (b) Centroid energy; (c) Proportion of pre-edge peak component at 7111.4 eV (P1); (d) Proportion of pre-edge peak component P3.

Figure 9. Orientation-corrected values of energy at $I_{\mathrm{N}} = 0.9$ plotted against Mössbauer-derived $\mathrm{Fe}^{3+}/\mathrm{Fe}_{\mathrm{tot}}$. Energy at $I_{\mathrm{N}} = 0.9$ values are corrected to a value of ϕ_{Z} using Eqn 4.

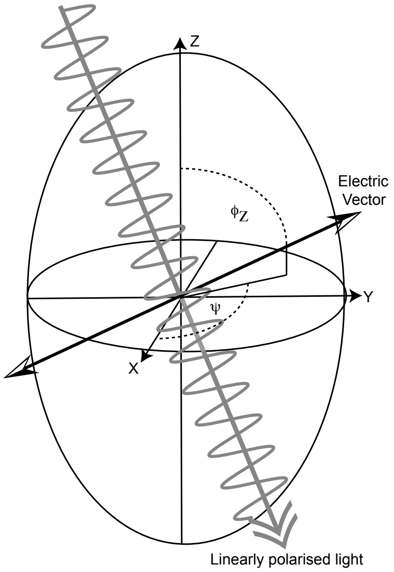

Figure 1:

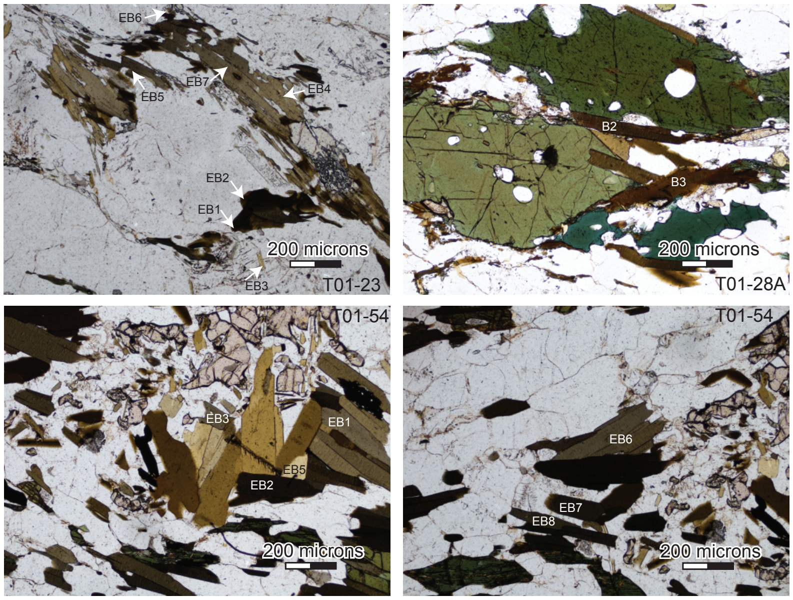
EB6
EB7
EB5
EB4
EB2
EB1
200 microns
EB3
T01-23
B2
B3
200 microns
T01-28A
T01-54
EB3
EB1
EB5
EB2
200 microns
T01-54
EB6
EB7
EB8
200 microns

Figure 2:

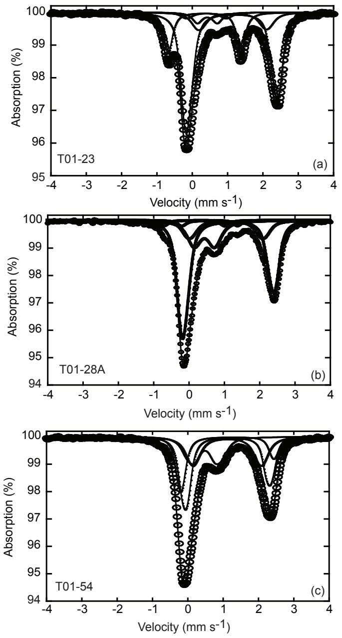
Absorption (%)
Velocity (mm s^{-1})
T01-23
(a)
T01-28A
(b)
T01-54
(c)
100
99
98
97
96
95
94
-4
-3
-2
-1
0
1
2
3
4

Figure 3:

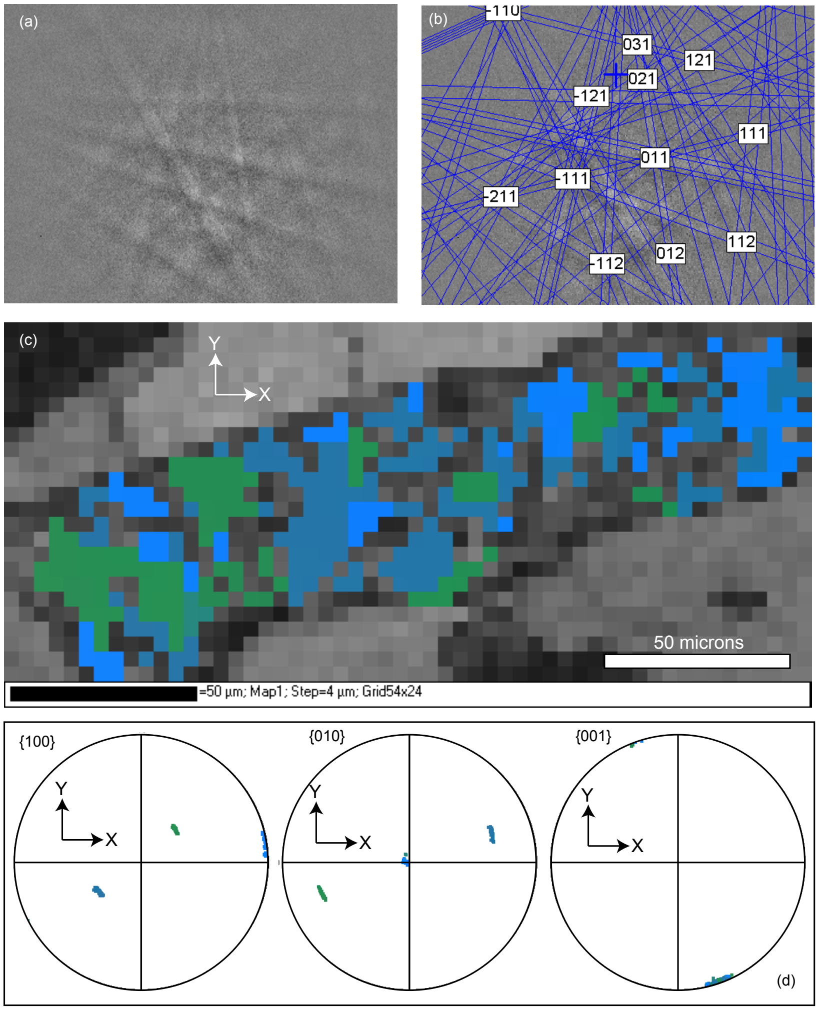
(a)
(b)
-110
031
121
021
-121
111
011
-111
-211
112
012
-112
(c)
Y
X
50 microns
=50 µm; Map1; Step=4 µm; Grid54x24
{100}
{010}
{001}
Y
X
(d)

Figure 4:

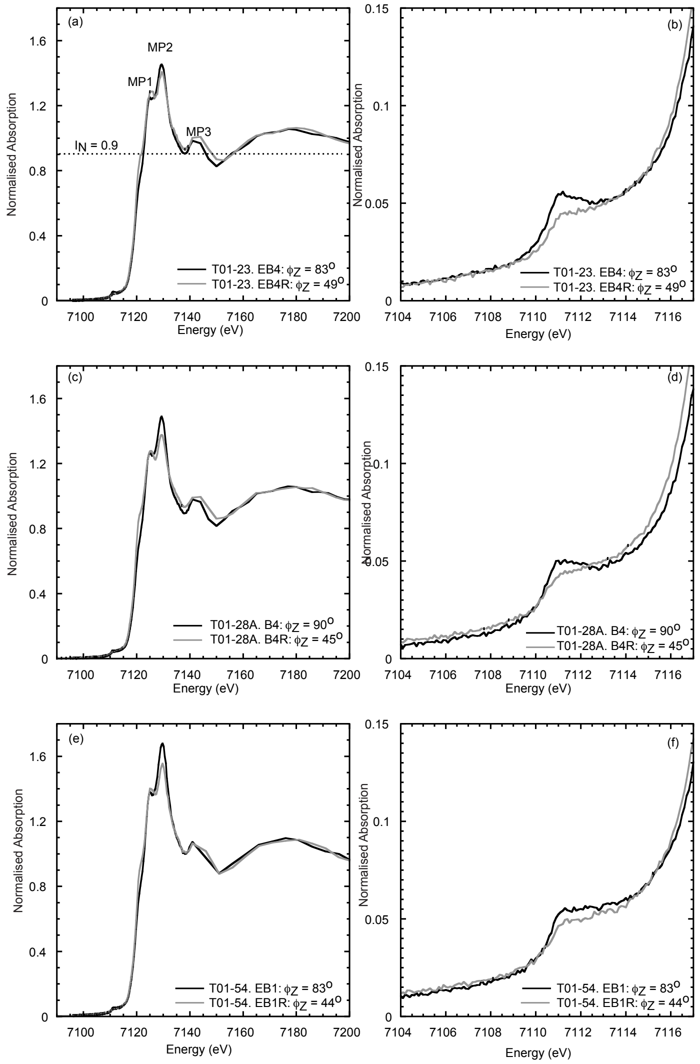
(a)
MP2
MP1
MP3
I_N = 0.9
Normalised Absorption
Energy (eV)
T01-23. EB4: ϕ_Z = 83°
T01-23. EB4R: ϕ_Z = 49°
(b)
T01-23. EB4: ϕ_Z = 83°
T01-23. EB4R: ϕ_Z = 49°
(c)
T01-28A. B4: ϕ_Z = 90°
T01-28A. B4R: ϕ_Z = 45°
(d)
T01-28A. B4: ϕ_Z = 90°
T01-28A. B4R: ϕ_Z = 45°
(e)
T01-54. EB1: ϕ_Z = 83°
T01-54. EB1R: ϕ_Z = 44°
(f)
T01-54. EB1: ϕ_Z = 83°
T01-54. EB1R: ϕ_Z = 44°
0
0.4
0.8
1.2
1.6
7100
7120
7140
7160
7180
7200
0.05
0.1
0.15
7104
7106
7108
7110
7112
7114
7116

Figure 5:

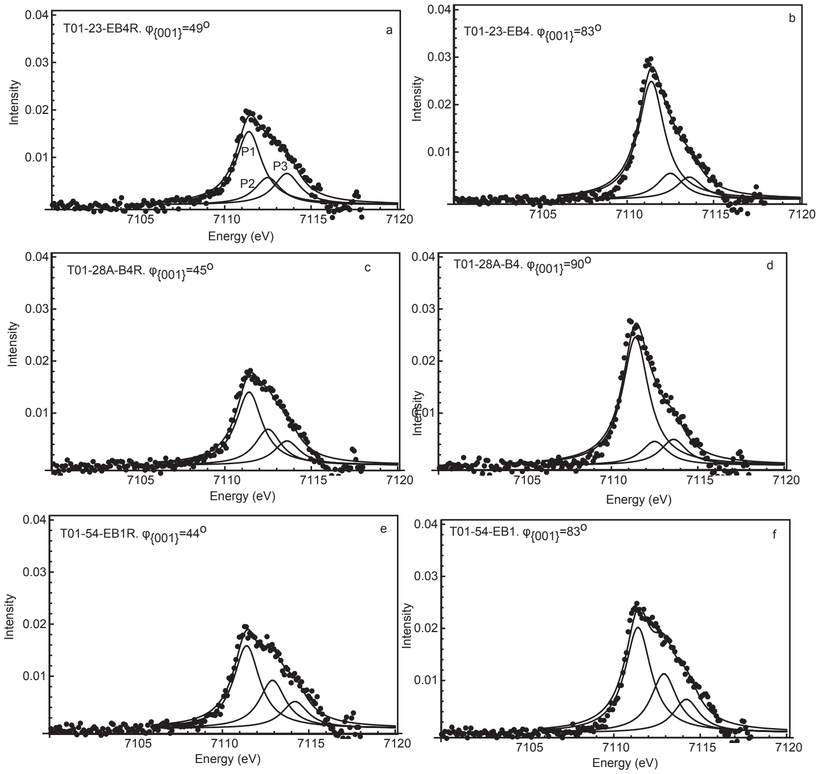T01-23-EB4R. φ{001}=49o
a
P1
P2
P3
T01-23-EB4. φ{001}=83o
b
T01-28A-B4R. φ{001}=45o
c
T01-28A-B4. φ{001}=90o
d
T01-54-EB1R. φ{001}=44o
e
T01-54-EB1. φ{001}=83o
f
Intensity
0.04
0.03
0.02
0.01
Energy (eV)
7105
7110
7115
7120

Figure 6:

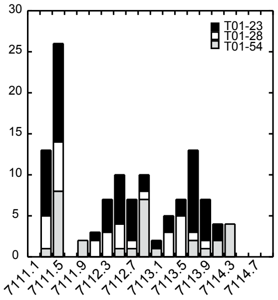
30
25
20
15
10
5
0
T01-23
T01-28
T01-54
7111.1
7111.5
7111.9
7112.3
7112.7
7113.1
7113.5
7113.9
7114.3
7114.7

Figure 7:

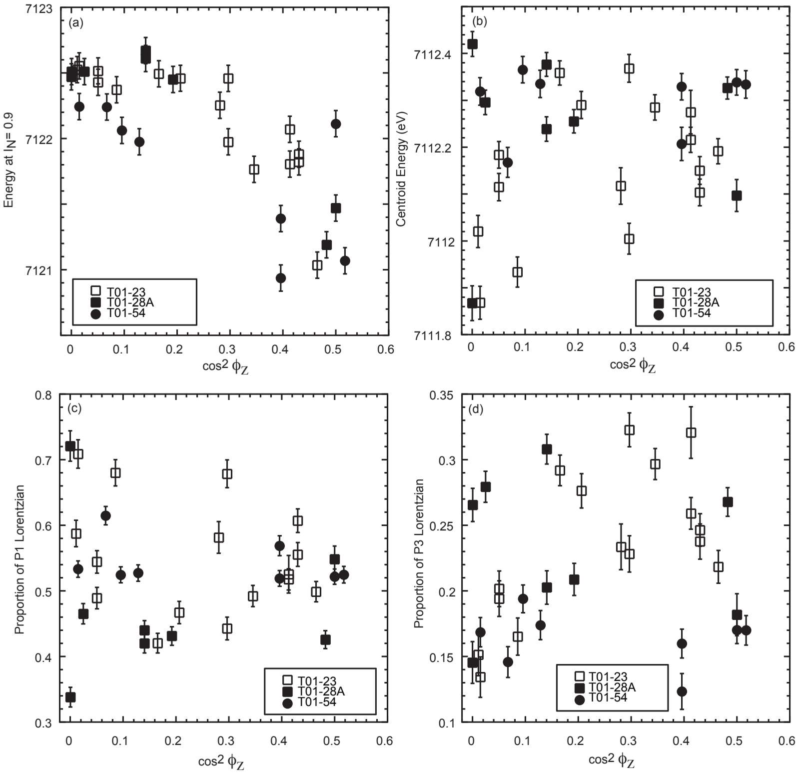
(a)
Energy at I_N= 0.9
7123
7122
7121
(b)
Centroid Energy (eV)
7112.4
7112.2
7112
7111.8
(c)
Proportion of P1 Lorentzian
0.8
0.7
0.6
0.5
0.4
0.3
(d)
Proportion of P3 Lorentzian
0.35
0.3
0.25
0.2
0.15
0.1
0
0.1
0.2
0.3
0.4
0.5
0.6
cos2 φZ
□ T01-23
■ T01-28A
● T01-54

Figure 8:

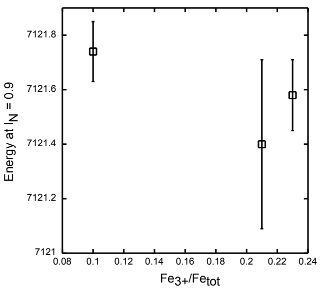
7121.8
7121.6
7121.4
7121.2
7121
Energy at I_N = 0.9
0.08
0.1
0.12
0.14
0.16
0.18
0.2
0.22
0.24
Fe3+/Fetot

Figure 9:

Tables

Table 1: T01-23 biotite composition data

wt% ox	EB1	σ	EB3	σ	EB4	σ	EB5	σ
SiO_2	35.84	0.30	36.13	0.16	35.65	0.35	36.22	0.55
TiO_2	2.61	0.03	2.54	0.01	2.66	0.03	2.81	0.02
Al_2O_3	16.40	0.19	15.70	0.03	15.83	0.09	15.95	0.02
Cr_2O_3	0.02	0.01	0.01	0.00	0.03	0.01	0.02	0.01
FeO	20.26	0.21	20.86	0.26	21.25	0.46	21.17	0.10
MnO	0.20	0.01	0.22	0.02	0.23	0.01	0.23	0.00
MgO	9.40	0.21	9.54	0.07	9.58	0.20	9.55	0.06
Na_2O	0.02	0.02	0.02	0.01	0.03	0.02	0.06	0.03
K_2O	6.87	0.87	9.16	0.10	9.14	0.11	9.04	0.15
Cl	0.51	0.02	0.49	0.01	0.51	0.01	0.49	0.01
F	0.14	0.12	0.13	0.20	0.14	0.07	0.12	0.06
H_2O	7.55	0.05	3.74	0.01	3.73	0.01	3.74	0.01
Total	99.82		98.54		98.78		99.40	
X(Mg)	0.45		0.45		0.45		0.45	
Fe^{3+}/Fe_{tot}	0.07		0.00		0.00		0.00	
Si	2.802		2.807		2.772		2.789	
Ti	0.153		0.148		0.156		0.163	
Al	1.511		1.438		1.452		1.448	
Cr	0.001		0.001		0.002		0.001	
Fe(III)	0.09		0		0		0	
Fe(II)	1.235		1.356		1.382		1.363	
Mn	0.013		0.014		0.015		0.015	
Mg	1.095		1.105		1.11		1.096	
Na	0.003		0.003		0.005		0.009	
K	0.685		0.908		0.907		0.888	
totals	7.589		7.781		7.802		7.773	

σ is the standard deviation on 3 – 5 measured points on each grain

Table 2: T01-28A biotite composition data

	B2	σ	B3	σ	B4	σ	B5	σ	B6	σ
SiO_2	36.31	0.26	36.68	0.11	36.92	0.16	36.57	0.14	36.15	0.35
TiO_2	2.81	0.08	2.86	0.03	2.76	0.03	2.89	0.04	2.39	0.05
Al_2O_3	15.51	0.14	15.48	0.07	15.57	0.20	15.29	0.03	15.37	0.15
Cr_2O_3	0.06	0.01	0.04	0.01	0.05	0.01	0.06	0.02	0.01	0.01
FeO	21.08	0.39	21.36	0.22	21.53	0.10	21.67	0.36	20.99	0.12
MnO	0.22	0.03	0.25	0.01	0.25	0.03	0.25	0.01	0.24	0.01
MgO	10.48	0.07	10.36	0.16	10.47	0.03	10.17	0.07	10.65	0.08
Na_2O	0.03	0.01	0.05	0.02	0.03	0.00	0.03	0.02	0.04	0.01
K_2O	8.78	0.22	7.64	0.10	8.95	0.28	9.12	0.37	8.48	0.16
Cl	0.25	0.02	0.24	0.00	0.25	0.01	0.24	0.01	0.25	0.02
F	0.10	0.08	0.18	0.04	0.17	0.08	0.09	0.11	0.26	0.12
H_2O	3.76	0.01	3.78	0.01	3.75	0.01	3.74	0.02	3.75	0.01
Total	99.39		98.93		100.70		100.12		98.58	
X(Mg)	0.47		0.47		0.47		0.46		0.48	
Fe^{3+}/Fe_{tot}	0.04		0.11		0.03		0.00		0.10	
Si	2.778		2.793		2.793		2.794		2.781	
Ti	0.161		0.164		0.157		0.166		0.138	
Al	1.399		1.39		1.389		1.377		1.394	
Cr	0.004		0.003		0.003		0.004		0.001	
Fe(III)	0.057		0.145		0.04		0.006		0.129	
Fe(II)	1.291		1.215		1.322		1.378		1.221	
Mn	0.015		0.016		0.016		0.016		0.016	
Mg	1.195		1.175		1.181		1.158		1.22	
Na	0.004		0.007		0.005		0.004		0.006	
K	0.857		0.743		0.864		0.889		0.832	
totals	7.762		7.651		7.77		7.794		7.739	

σ is the standard deviation on 3 – 5 measured points on each grain, except B6 which has only two good analyses

Table 3: T01-54 biotite composition data

	B1	σ	B2	σ	B4	σ	B5	σ	B6	σ	B7	σ	B8	σ
SiO_2	36.29	0.08	36.29	0.29	37.24	0.29	37.16	0.30	36.74	0.16	37.05	0.21	36.75	0.28
TiO_2	3.96	0.05	3.97	0.05	3.96	0.20	3.98	0.05	4.19	0.09	3.94	0.08	3.93	0.06
Al_2O_3	14.84	0.07	14.79	0.10	15.42	0.62	15.01	0.08	15.25	0.18	14.71	0.06	14.76	0.07
Cr_2O_3	0.06	0.02	0.07	0.01	0.07	0.01	0.08	0.01	0.07	0.02	0.06	0.03	0.06	0.02
FeO	17.87	0.15	18.25	0.55	18.12	0.47	17.76	0.16	17.76	0.29	18.48	0.45	18.39	0.66
MnO	0.05	0.01	0.03	0.01	0.01	0.01	0.03	0.01	0.02	0.01	0.05	0.02	0.04	0.02
MgO	12.71	0.07	12.78	0.08	11.90	0.92	12.57	0.05	12.39	0.19	12.58	0.04	12.60	0.04
Na_2O	0.03	0.01	0.04	0.01	0.04	0.02	0.04	0.01	0.03	0.02	0.03	0.03	0.03	0.01
K_2O	8.59	0.15	8.72	0.22	8.67	0.34	8.87	0.48	8.74	0.11	8.79	0.25	8.94	0.14
Cl	0.49	0.02	0.48	0.01	0.50	0.02	0.47	0.02	0.48	0.02	0.47	0.01	0.47	0.01
F	0.38	0.11	0.43	0.11	0.26	0.11	0.37	0.07	0.41	0.12	0.34	0.16	0.36	0.04
H_2O	3.79	0.01	3.77	0.01	3.80	0.01	3.79	0.01	3.79	0.01	3.78	0.01	3.77	0.01
Total	99.05		99.63		100.00		100.13		99.88		100.27		100.10	
X(Mg)	0.56		0.56		0.54		0.56		0.56		0.55		0.55	
Fe^{3+}/Fe_{tot}	0.05		0.07		0.00		0.00		0.00		0.01		0.02	
Si	2.76		2.749		2.801		2.795		2.772		2.79		2.776	
Ti	0.227		0.226		0.224		0.225		0.238		0.223		0.223	
Al	1.33		1.32		1.367		1.331		1.357		1.306		1.315	
Cr	0.003		0.004		0.004		0.005		0.004		0.004		0.004	
Fe(III)	0.056		0.078		0		0		0		0.016		0.018	
Fe(II)	1.08		1.078		1.14		1.117		1.121		1.147		1.144	
Mn	0.003		0.002		0.001		0.002		0.001		0.003		0.003	
Mg	1.44		1.443		1.333		1.409		1.394		1.411		1.418	
Na	0.004		0.005		0.006		0.005		0.005		0.005		0.004	
K	0.833		0.843		0.832		0.851		0.841		0.844		0.861	
totals	7.738		7.749		7.708		7.741		7.733		7.75		7.766	

σ is the standard deviation on 3 – 5 measured points on each grain

Table 4: Mössbauer data

		T01-23	T01-28A	T01-54
Fe^{2+} in biotite	δ			1.13
	Δ			2.34
	Γ			0.24
	area			36
Fe^{2+} in biotite	δ	1.13	1.13	1.13
	Δ	2.6	2.61	2.63
	Γ	0.24	0.24	0.24
	area	58	60	20
Fe^{2+} in biotite	δ	1.15	1.07	1.12
	Δ	1.98	2.09	1.97
	Γ	0.38	0.35	0.4
	area	13	15	23
Fe^{3+} in biotite	δ	0.43	0.45	0.48
	Δ	0.56	0.57	0.58
	Γ	0.3	0.41	0.34
	area	6	20	21
Fe^{2+} in biotite	δ	0.4	0.42	
	Δ	1.14	1.22	
	Γ	0.37	0.3	
	area	4	3	
Center 2 peaks from Fe^{3+} oxide	δ	0.35	0.35	
	Δ	2.04	2.08	
	Γ	0.24	0.24	
	area	19	3	
	χ^2	0.99	0.85	1.15
$\%Fe^{3+}$ in biotite		10	23	21
σ $\%Fe^{3+}$ in biotite		2	2	2

Table 5: Orientation and XANES parameters for T01-23

Grain	E (eV)	ϕ_Z	Area	Area	Area	σ	σ	σ	centroid	σ	$\frac{Fe^{3+}}{Fe_{tot}}$	σ	Prop	Prop	Prop
	@I_N=0.9		P1	P2	P3	P1	P2	P3	(eV)	centroid	mol %	$\frac{Fe^{3+}}{Fe_{tot}}$	P1	P2	P3
T01-23-EB9r	7121.04	47	0.061	0.034	0.027	0.002	0.003	0.002	7112.19	0.03	14.6	1.5	0.50	0.28	0.22
T01-23-EB4r	7121.82	49	0.063	0.023	0.027	0.002	0.003	0.002	7112.15	0.03	12.6	1.5	0.56	0.21	0.24
T01-23-EB5r	7121.88	49	0.073	0.018	0.030	0.002	0.003	0.002	7112.10	0.03	10.3	1.4	0.61	0.15	0.25
T01-23-EB10r	7121.80	50	0.068	0.029	0.034	0.002	0.003	0.002	7112.22	0.03	15.8	1.3	0.52	0.22	0.26
T01-23-EB8r	7122.07	50	0.057	0.017	0.035	0.003	0.004	0.003	7112.27	0.05	18.7	2.3	0.53	0.15	0.32
T01-23-EB1r	7121.76	54	0.063	0.027	0.038	0.002	0.003	0.002	7112.28	0.03	19.2	1.3	0.49	0.21	0.30
T01-23-EB1	7122.46	57	0.050	0.026	0.036	0.002	0.003	0.002	7112.37	0.03	23.3	1.5	0.44	0.23	0.32
T01-23-EB3r	7121.97	57	0.089	0.012	0.030	0.002	0.003	0.002	7112.00	0.03	5.4	1.6	0.68	0.09	0.23
T01-23-EB2r	7122.25	58	0.068	0.022	0.027	0.003	0.004	0.003	7112.12	0.04	11.0	1.9	0.58	0.18	0.23
T01-23-EB2	7122.46	63	0.058	0.032	0.034	0.002	0.003	0.002	7112.29	0.03	19.5	1.4	0.47	0.26	0.28
T01-23-EB3	7122.49	66	0.066	0.045	0.046	0.003	0.003	0.003	7112.36	0.03	22.9	1.3	0.42	0.29	0.29
T01-23-EB9	7122.37	73	0.102	0.023	0.025	0.003	0.003	0.003	7111.93	0.03	1.9	1.6	0.68	0.15	0.17
T01-23-EB10	7122.43	77	0.081	0.039	0.029	0.002	0.003	0.002	7112.11	0.03	10.8	1.4	0.54	0.26	0.19
T01-23-EB5	7122.52	77	0.074	0.047	0.030	0.003	0.003	0.003	7112.18	0.03	14.2	1.4	0.49	0.31	0.20
T01-23-EB4	7122.55	83	0.102	0.022	0.019	0.003	0.003	0.003	7111.87	0.04	-1.3	1.7	0.71	0.16	0.13
T01-23-EB8	7122.52	84	0.082	0.036	0.021	0.003	0.004	0.003	7112.02	0.03	6.2	1.7	0.59	0.26	0.15
Average			0.072	0.028	0.030				7112.15		12.8		0.55	0.21	0.24
1σ			0.015	0.010	0.007				0.15		7.2		0.09	0.06	0.06

Table 6: Orientation and XANES parameters for T01-28A

Grain	E (eV)	ϕ_Z	Area	Area	Area	σ	σ	σ	centroid	σ	$\frac{Fe^{3+}}{Fe_{tot}}$	σ	Prop	Prop	Prop
	@I_N=0.9		P1	P2	P3	P1	P2	P3	(eV)	centroid	mol %	$\frac{Fe^{3+}}{Fe_{tot}}$	P1	P2	P3
T01-28A-B4r	7121.47	45	0.057	0.028	0.019	0.002	0.003	0.002	7112.10	0.03	9.9	1.7	0.55	0.27	0.18
T01-28A-B3	7121.19	46	0.064	0.046	0.041	0.002	0.003	0.002	7112.33	0.02	21.3	1.2	0.43	0.31	0.27
T01-28A-B5	7122.45	64	0.068	0.056	0.033	0.002	0.003	0.002	7112.26	0.03	17.8	1.2	0.43	0.36	0.21
T01-28A-B5r	7122.61	68	0.060	0.038	0.044	0.002	0.003	0.002	7112.38	0.03	23.8	1.3	0.42	0.27	0.31
T01-28A-B6	7122.67	68	0.065	0.053	0.030	0.002	0.003	0.002	7112.24	0.03	17.0	1.3	0.44	0.36	0.20
T01-28A-B6r	7122.51	81	0.057	0.031	0.034	0.002	0.003	0.002	7112.30	0.03	19.8	1.3	0.47	0.26	0.28
T01-28A-B3r	7122.51	89	0.047	0.055	0.037	0.002	0.003	0.002	7112.42	0.03	25.9	1.3	0.34	0.40	0.27
T01-28A-B4	7122.47	90	0.100	0.019	0.020	0.003	0.003	0.003	7111.87	0.04	-1.4	1.8	0.72	0.13	0.15
Average			0.065	0.041	0.032				7112.23		16.7		0.47	0.29	0.23
1σ			0.016	0.014	0.009				0.18		8.8		0.12	0.08	0.06

Table 7: Orientation and XANES parameters for T01-54

Grain	E (eV) @I_N=0.9	ϕ_Z	Area P1	Area P2	Area P3	σ P1	σ P2	σ P3	centroid (eV)	σ centroid	$\frac{Fe^{3+}}{Fe_{tot}}$ mol %	σ $\frac{Fe^{3+}}{Fe_{tot}}$	Prop P1	Prop P2	Prop P3
T01-54-EB1r	7121.07	44	0.065	0.038	0.021	0.002	0.002	0.002	7112.33	0.03	21.6	1.5	0.52	0.31	0.17
T01-54-EB5	7122.11	45	0.079	0.047	0.026	0.002	0.002	0.002	7112.34	0.03	21.9	1.3	0.52	0.31	0.17
T01-54-EB2r	7120.94	51	0.069	0.037	0.015	0.002	0.002	0.002	7112.21	0.04	15.4	1.8	0.57	0.31	0.12
T01-54-EB6r	7121.39	51	0.070	0.043	0.022	0.002	0.002	0.002	7112.33	0.03	21.4	1.4	0.52	0.32	0.16
T01-54-EB6	7121.98	69	0.077	0.044	0.025	0.002	0.002	0.002	7112.34	0.03	21.7	1.4	0.53	0.30	0.17
T01-54-EB5r	7122.06	72	0.083	0.045	0.031	0.002	0.002	0.002	7112.37	0.03	23.2	1.4	0.52	0.28	0.19
T01-54-EB2	7122.24	75	0.087	0.034	0.021	0.002	0.002	0.002	7112.17	0.03	13.4	1.6	0.61	0.24	0.15
T01-54-EB1	7122.24	83	0.082	0.046	0.026	0.002	0.002	0.002	7112.32	0.03	20.9	1.4	0.53	0.30	0.17
Average			0.076	0.042	0.023				7112.30		20.0		0.54	0.29	0.16
1σ			0.008	0.005	0.005				0.07		3.5		0.03	0.03	0.02

Table 8: Correlation information.

		T01-23		T01-28A		T01-54	
		(I_N=0.9	$\cos^2\phi_{\{Z\}}$	I_N=0.9	$\cos^2\phi_{\{Z\}}$	I_N=0.9	$\cos^2\phi_{\{Z\}}$
$\cos^2\phi_{\{Z\}}$	Pearson Correlation Coefficient	-0.844	n.a.	-0.918	n.a.	-0.681	n.a.
	p-value	0.00004	n.a.	0.001	n.a.	0.063	n.a.
Area (P1)	Pearson Correlation Coefficient	0.369	-0.624	0.085	-0.197	0.915	-0.788
	p-value	0.160	0.010	0.841	0.640	0.001	0.020
Area (P2)	Pearson Correlation Coefficient	0.279	-0.467	0.094	0.013	0.482	-0.086
	p-value	0.296	0.068	0.824	0.976	0.226	0.840
Area (P3)	Pearson Correlation Coefficient	-0.037	0.312	0.128	-0.091	0.761	-0.439
	p-value	0.893	0.239	0.763	0.830	0.028	0.277
Centroid	Pearson Correlation Coefficient	-0.176	0.434	0.081	0.005	0.191	0.143
	p-value	0.515	0.093	0.849	0.990	0.650	0.736
Total Area	Pearson Correlation Coefficient	0.526	-0.781	0.225	-0.220	0.932	-0.618
	p-value	0.036	0.0004	0.592	0.600	0.001	0.102
Proportion (P1)	Pearson Correlation Coefficient	0.100	-0.247	-0.065	-0.039	0.020	-0.325
	p-value	0.713	0.357	0.879	0.926	0.962	0.432
Proportion (P2)	Pearson Correlation Coefficient	0.101	-0.247	0.022	0.100	-0.477	0.622
	p-value	0.711	0.356	0.958	0.814	0.232	0.100
Proportion (P3)	Pearson Correlation Coefficient	-0.257	0.632	0.100	-0.066	0.536	-0.224
	p-value	0.337	0.009	0.813	0.877	0.171	0.593

Table 9: Orientation correction function information

	T01-23	T01-28	T01-54
$m(I_{\mathrm{N}} = 0.9$	-2.25	-2.52	-1.91
$\sigma_{m(I_{\mathrm{N}}=0.9}$	0.38	0.45	0.84
$c(I_{\mathrm{N}} = 0.9$	7122.87	7122.85	7122.35
$\sigma_{c(I_{\mathrm{N}}=0.9}$	0.11	0.12	0.27
$I_{\mathrm{N}} = 0.9$ @ 45^o	7121.74	7121.58	7121.40
$\sigma_{I_{\mathrm{N}}=0.9}$ @ 45^o	0.11	0.13	0.31

Further references:

Garvie, L.A.J., Zega, T.J., Rez, P., and Buseck, P.R. (2004) Nanometer-scale measurements of Fe3+/ΣFe by electron energy-loss spectroscopy: A cautionary note. American Mineralogist, 89, 1610–1616.

Keast, V.J., Scott, A.J., Brydson, R., Williams, D.B., and Bruley, J. (2001) Electron energy-loss near-edge structure—a tool for the investigation of electronic structure on the nanometre scale. Journal of Microscopy, 203, 135–175.

McCammon, C. (2005) Mantle oxidation state and oxygen fugacity: constraints on mantle chemistry, structure and dynamics. In R.D. van der Hilst, J.D. Bass, J. Matas, and J. Trampert, Eds., Earth’s Deep Mantle: Structure, composition and evolution, 160, p. 219–240. AGU, Washington D.C.

McCammon, C.A., Frost, D.J., Smyth, J.R., Laustsen, H.M.S., Kawamoto, T., Ross, N.L., and van Aken, P.A. (2004) Oxidation state of iron in hydrous mantle phases: implications for subduction and mantle oxygen fugacity. Physics of the Earth and Planetary Interiors, 143-44, 157–169.